Corridor 3D Navigation of a Fully-Actuated Multirotor by Means of Bee-Inspired Optic Flow Regulation

José de Jesus Castillo-Zamora, Lucia Bergantin, Franck Ruffier

Corridor 3D Navigation of a Fully-Actuated Multirotor by Means of Bee-Inspired Optic Flow Regulation

Jose J. Castillo-Zamora[1,*], Lucia Bergantin[1], Franck Ruffier[1]

Abstract

This paper deals with the issue of autonomous indoors navigation related to Unmanned Aerial Vehicles. Here, we simulated two hexarotors: a fully-actuated one that maintains level its attitude, and therefore that of the visual sensors; and an under-actuated one. Both vehicles were meant to fly forwards in a tunnel while reacting to the irregularities of the terrain, adopting a bee-like behavior based on a nonlinear optic flow regulation. The dynamic models are provided by means of the Newton-Euler equations, nonetheless, the unit quaternion representation is used for a suitable treatment of the rotational motion. The attitude stabilization depends on the knowledge of the quaternion itself, moreover, and due to the non-linearities related to the translational optic flows, visual guidance relies on the implementation of adaptive integral sliding mode controllers to accomplish a triple direct regulation (forward, side and lift commands). We compared both vehicles performance using detailed numerical simulations, validating the concept that a fully actuated hexarotor permits to improve the optic flow based navigation task.

I. Introduction

Nowadays, it is evident to appreciate the enlargement of the application spectrum of Unmanned Aerial Vehicles (UAVs) within several scientific, industrial or civil fields. The current technological raise enables these small scale vehicles to be used in order to accomplish different tasks that include photography, surveillance, monitoring, parcel transport and delivery, and environmental exploration, among others.

Amidst the aforementioned tasks, indoors autonomous exploration has been under the sight of the scientific community since it implies overcoming diverse challenges as openings identification [1], intersections and dead-ends detection [2], obstacle avoidance [3], to mention some.

During these operations, the implementation of visual-servoing techniques and vision-based algorithms becomes a matter of crucial importance since, in most indoor environments, Global Navigation Satellite Systems (GNSS) are unavailable [4]. In this regard, one of the most useful visual cues is the so-called *Optic Flow* (OF). Previous studies have suggested that OF is used by winged insects, such as honeybees and moths, to perform several complicated tasks as take-off and landing, undesired wind effects rejection, corridor navigation, etc [5], [6].

The latter has led to the development of bio-inspired vision-based controllers for various robotic systems including aerial robots [7], [8], [9]. Moreover, the authors of [10] have used *OF divergence* to asses, via an Extended Kalman Filter (EKF), the distance from a given surface by means of two OF sensors set on a back-and-forth oscillating chariot. In [11], a model of the honeybee's visual odometer is assessed in simulations by scaling of the integration of the translational OF via the estimation of the flight height.

One may find that OF can be confidently used in conjunction with other control and navigation techniques (e.g. Fuzzy Logic [12] and real-time way-point-based 3D local path planning [13]) to enhance the navigation capabilities of UAVs. In addition, the literature also suggests that, even for outdoors applications where GNSS are enable, OF is a powerful data source since it permits to improve the reliability of flight controllers [14], [15].

It is known that co-planar multirotors need bulky gimbal systems to stabilize their vision. In this sense, we simulated a fully-actuated hexarotor that maintains level its attitude and that of the OF sensors while flying forwards in a corridor. The novelty of the paper comprehends (i) the development of Adaptive Integral Sliding Mode Controllers (AI-SMCs) for a Fully-Actuated Hexarotor and (ii) the merging of the Fully-Actuation advantages with those of the Optic Flow regulation in a 3D environment, such that a bio-inspired corridor navigation strategy grants the UAV a bee-like behavior.

The detailed description of the vehicle dynamics is available in Section II. The navigation strategy, which comprehends the optic flow regulation and the attitude stabilization in a corridor, is established in Section III. The simulation conditions and parameters, as well as the discussion of the results, are given in Section IV. Lastly, the future work and concluding remarks are comprised in Section V.

II. Fully-Actuated Hexarotor (FAH) Model

The current section is devoted to provide the equations of motion of the Fully-Actuated Hexarotor (FAH) depicted in Fig. 1. Full-actuation is achieved by a fixed tilted rotors configuration as explained in [16], [17], [18]. The dynamics of the vehicle is described w.r.t. two reference frames: (i) the inertial frame $O_I\{x_I, y_I, z_I\}$, and (ii) the body frame $O_b\{x_b, y_b, z_b\}$ whose origin

[1] Aix-Marseille Université, CNRS, ISM, Marseille, France
[*] Corresponding author: jose-de-jesus.castillo-zamora@univ-amu.fr

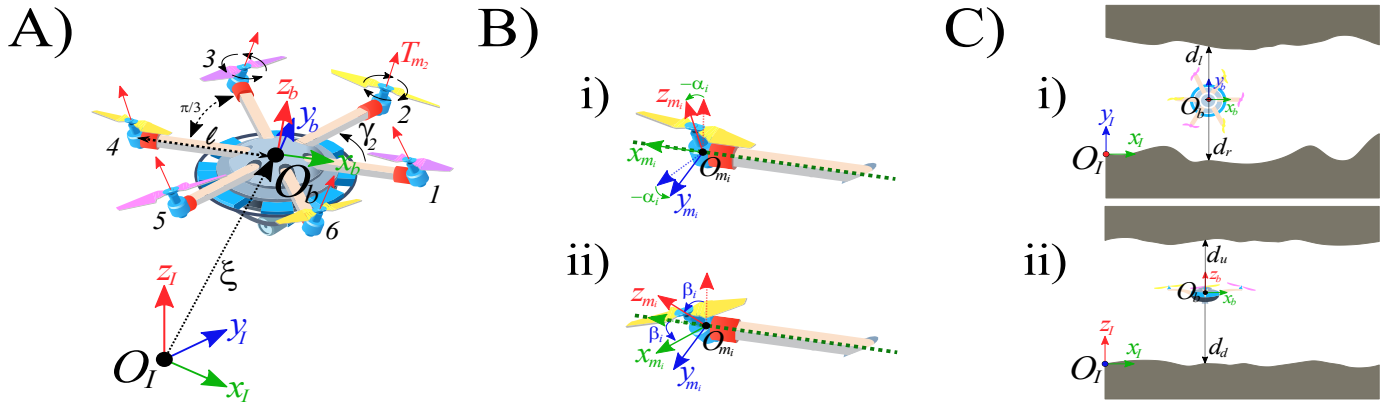

Figure 1. A) FAH geometrical description. B) Angles of the fixed tilted rotors. C) FAH in a corridor.

coincides with the center of gravity (CoG). x_b, y_b and z_b define, correspondingly, the roll, pitch and yaw axis which are aligned to the reciprocal principal axis of inertia. Thus, the motion of the FAH is described by the Newton Euler formulation [19] as:

$$m\ddot{\boldsymbol{\xi}} + m\mathbf{g} = \boldsymbol{\tau}_{\boldsymbol{\xi}} + \boldsymbol{\rho}_{\boldsymbol{\xi}} \tag{1}$$

$$I\dot{\boldsymbol{\Omega}} + \boldsymbol{\Omega} \times (I\boldsymbol{\Omega}) = \boldsymbol{\tau}_{\boldsymbol{\Omega}} + \boldsymbol{\rho}_{\boldsymbol{\Omega}} \tag{2}$$

where $m > 0$ is the mass of the vehicle, $I = \text{diag}\,(I_x, I_y, I_z) \in \mathbb{R}^{3\times3}$ is the inertia matrix which gathers the moments of inertia about the roll, pitch and yaw axis, respectively. $\mathbf{g} = [0\ 0\ g]^T$ comprises the constant of gravity acceleration and $\boldsymbol{\rho}_{\boldsymbol{\xi}},\ \boldsymbol{\rho}_{\boldsymbol{\Omega}} \in \mathbb{R}^3$ represent parametric/external disturbances.

A. Translational dynamics

The translational motion is described by Eq. (1) where $\boldsymbol{\xi} = [x\ y\ z]^T \in \mathbb{R}^3$ denotes the position of O_b w.r.t. O_I. Thus, $\dot{\boldsymbol{\xi}}$ and $\ddot{\boldsymbol{\xi}}$ stand for the velocity and acceleration, respectively. $\boldsymbol{\tau}_{\boldsymbol{\xi}} \in \mathbb{R}^3$ is the vector of external forces, defined by the forces $T_m^u \geq T_{m_i} \geq 0$ (with $i = 1, 2, ..., 6$ and T_m^u an upper bound) exerted by the actuators as:

$$\boldsymbol{\tau}_{\boldsymbol{\xi}} = [\tau_x\ \tau_y\ \tau_z]^T = R_{\boldsymbol{\eta}} \sum_{i=1}^{6} R_{\boldsymbol{\eta}_{m_i}} [0\ 0\ T_{m_i}]^T \tag{3}$$

Furthermore, the rotation matrix $R_{\boldsymbol{\nu}} \in \mathbb{R}^{3\times3}$, defined over a given vector $\boldsymbol{\nu} = [\nu_1\ \nu_2\ \nu_3]^T \in \mathbb{R}^3$ as:

$$R_{\boldsymbol{\nu}} = R_{3,\nu_3} R_{2,\nu_2} R_{1,\nu_1} = \tag{4}$$
$$\begin{bmatrix} \mathrm{C}_{\nu_3} & -\mathrm{S}_{\nu_3} & 0 \\ \mathrm{S}_{\nu_3} & \mathrm{C}_{\nu_3} & 0 \\ 0 & 0 & 1 \end{bmatrix} \begin{bmatrix} \mathrm{C}_{\nu_2} & 0 & \mathrm{S}_{\nu_2} \\ 0 & 1 & 0 \\ -\mathrm{S}_{\nu_2} & 0 & \mathrm{C}_{\nu_2} \end{bmatrix} \begin{bmatrix} 1 & 0 & 0 \\ 0 & \mathrm{C}_{\nu_1} & -\mathrm{S}_{\nu_1} \\ 0 & \mathrm{S}_{\nu_1} & \mathrm{C}_{\nu_1} \end{bmatrix}$$

with $\mathrm{C}_\bullet = \cos(\bullet)$ and $\mathrm{S}_\bullet = \sin(\bullet)$, provides a vector mapping from a reference frame to another. $R_{\boldsymbol{\eta}_{m_i}}$ provides a vector mapping from the $i-th$ motor reference frame $O_{m_i}\{x_{m_i}, y_{m_i}, z_{m_i}\}$ to O_b such that $\boldsymbol{\eta}_{m_i} = [\alpha_i\ \beta_i\ \gamma_i]^T \in \mathbb{R}^3$ comprises the fixed tilted angles α_i and β_i, and $\gamma_i = (i-1)\pi/3$ that is related to the geometry of the FAH (Fig. 1). $R_{\boldsymbol{\eta}}$ maps a vector described in O_b to O_I and it depends on the attitude of the vehicle defined by the Euler angles $\boldsymbol{\eta} = [\phi\ \theta\ \psi]^T \in \mathbb{R}^3$.

B. Rotational dynamics

The rotational motion is described in the body frame by Eq. (2). The angular velocity vector $\boldsymbol{\Omega} = [p\ q\ r]^T \in \mathbb{R}^3$ is related to the Euler rates $\dot{\boldsymbol{\eta}}$ in the sense that:

$$\boldsymbol{\Omega} = W_{\boldsymbol{\eta}} \dot{\boldsymbol{\eta}}\ ;\ W_{\boldsymbol{\eta}} = \begin{bmatrix} 1 & 0 & -\mathrm{S}_\theta \\ 0 & \mathrm{C}_\phi & \mathrm{S}_\phi \mathrm{C}_\theta \\ 0 & -\mathrm{S}_\phi & \mathrm{C}_\phi \mathrm{C}_\theta \end{bmatrix} \in \mathbb{R}^{3\times3} \tag{5}$$

The vector $\boldsymbol{\tau}_{\boldsymbol{\Omega}} \in \mathbb{R}^3$ gathers the torques exerted by the propellers over the vehicle and it reads as:

$$\boldsymbol{\tau}_{\boldsymbol{\Omega}} = \begin{bmatrix}\tau_\phi & \tau_\theta & \tau_\psi\end{bmatrix}^T = \sum_{i=1}^{6} T_{m_i}\left\{\zeta R_{\boldsymbol{\eta}_{m_i}}\begin{bmatrix}0 & 0 & (-1)^{i-1}\end{bmatrix}^T + \ell\left(R_{3,\gamma_i}\begin{bmatrix}1 & 0 & 0\end{bmatrix}^T\right)\times\left(R_{\boldsymbol{\eta}_{m_i}}\begin{bmatrix}0 & 0 & 1\end{bmatrix}^T\right)\right\} \tag{6}$$

where $\ell > 0$ denotes the arm length and $\zeta > 0$ is a proportionality constant that relates the force T_{m_i} to the corresponding free moment such that $\tau_{m_i} = \zeta T_{m_i}$. The sign of the free moment is determined by the sense of rotation of the propellers (Fig. 1): the purple blades rotate anticlockwise (positive) and the yellow propellers rotate clockwise (negative).

C. Under-Actuated Hexarotor (UAH) model

Two different hexarotors are included in the study: (i) a FAH (Fig. 1), and (ii) an Under-Actuated Hexarotor (UAH). The UAH dynamics can be derived from Eqs. (1) and (2) while considering $\alpha_i = \beta_i = 0^\circ$ [20], [21]. For the UAH, ϕ and θ are used to drive the system in the space, thus:

$$\phi_d = \text{atan}\left(\frac{\tau_x S_\psi - \tau_y C_\psi}{\sqrt{\tau_z{}^2 + \left(\tau_x C_\psi + \tau_y S_\psi\right)^2}}\right) \tag{7}$$

$$\theta_d = \text{atan}\left(\left(\tau_x C_\psi + \tau_y S_\psi\right)/\tau_z\right) \tag{8}$$

D. Unit quaternion representation

To avoid any possible singularity, the unit quaternion representation [22], [23], [24] is adopted instead. Consider the orthogonal right-handed coordinate frames O_b and O_I, the rotation of O_b w.r.t. O_I can be parameterized in terms of a rotation $\vartheta \in \mathbb{R}$ about a fixed axis $\mathbf{e}_v \in \mathbb{S}^2 \subset \mathbb{R}^3$ by the mapping $\mathscr{U} : \mathbb{R}\times\mathbb{S}^2 \to SO(3)$ as:

$$\mathscr{U}(\vartheta, \mathbf{e}_v) = I_{3\times 3} + \mathrm{S}_\vartheta[\mathbf{e}_v^\times] + (1 - \mathrm{C}_\vartheta)[\mathbf{e}_v^\times]^2 \tag{9}$$

such that $I_{3\times 3} \in \mathbb{R}^{3\times 3}$ stands for the identity matrix and $[\mathbf{e}_v^\times]$ represents the well known skew-symmetric matrix of $\mathbf{e}_v$. Hence, a unit quaternion, $\mathbf{q} \in \mathbb{S}^3 \subset \mathbb{R}^4$, is defined as

$$\mathbf{q} = \begin{bmatrix}\mathrm{C}_{\vartheta/2} & \mathrm{S}_{\vartheta/2}\mathbf{e}_v^T\end{bmatrix}^T = \begin{bmatrix}q_0 & \mathbf{q}_v^T\end{bmatrix}^T \tag{10}$$

where $q_0 \in \mathbb{R}$ and $\mathbf{q}_v = \begin{bmatrix}q_1 & q_2 & q_3\end{bmatrix}^T \in \mathbb{R}^3$ are known as the scalar and vector parts of the quaternion, respectively. The rotation matrix in Eq. (4) can be rewritten in terms of $\mathbf{q}$ as:

$$R_{\mathbf{q}} = I_{3\times 3} + 2\left(q_0[\mathbf{q}_v^\times] + [\mathbf{q}_v^\times]^2\right) \tag{11}$$

Notice that $\mathbf{q}$ and $-\mathbf{q}$ represent the same physical attitude, i.e. $R_{\mathbf{q}} = R_{-\mathbf{q}}$. The latter equally serves to compute $\boldsymbol{\eta}$ from $\mathbf{q}$ and vice-versa. Finally, the quaternion propagation rule establishes the relation between $\dot{\mathbf{q}}$ and $\boldsymbol{\Omega}$:

$$\dot{\mathbf{q}} = \begin{bmatrix}\dot{q}_0 \\ \dot{\mathbf{q}}_v\end{bmatrix} = \frac{1}{2}\begin{bmatrix}-\mathbf{q}_v^T \\ I_{3\times 3}q_0 + [\mathbf{q}_v^\times]\end{bmatrix}\boldsymbol{\Omega} = \frac{1}{2}\Xi_{\mathbf{q}}\boldsymbol{\Omega} \tag{12}$$

which permits to describe the navigation strategy as follows.

III. Optic Flow-Based Navigation Strategy

This section provides a full description of the corridor navigation strategy depicted in Fig. 2. In the case of the FAH, the 4 OF sensors are rigidly attached to the body. In the case of the UAH, the 4 OF sensors are considered perfectly stabilized by means of a bulky gimbal system, for instance. The strategy proposal is inspired by a vision-based autopilot of a virtual bee that travels along a tunnel [25].

According to [25], it has been shown that the hymenopterans and the blowflies stabilize their gaze by compensating for any rotation. Therefore, it is assumed that the vehicle attitude is firstly stabilized at $\mathbf{q}_s = \begin{bmatrix}1 & 0 & 0 & 0\end{bmatrix}^T$ such that no rotational motion is experienced by the vehicle, thus stabilizing the OF sensors such that both vehicles (FAH and UAH) receive a purely translational OF defined as:

$$\omega_j = \dot{x}/d_j \quad \text{with } j \in \{r, l, u, d\} \tag{13}$$

where $\dot{x}$ is the forward speed if $\mathbf{q} \approx \mathbf{q}_s$, and d_j denotes the distance to the corresponding surface (see Fig. 1). Due to the non-linear dynamics and the non-linearities related to the OF, a sliding mode technique was applied as follows.

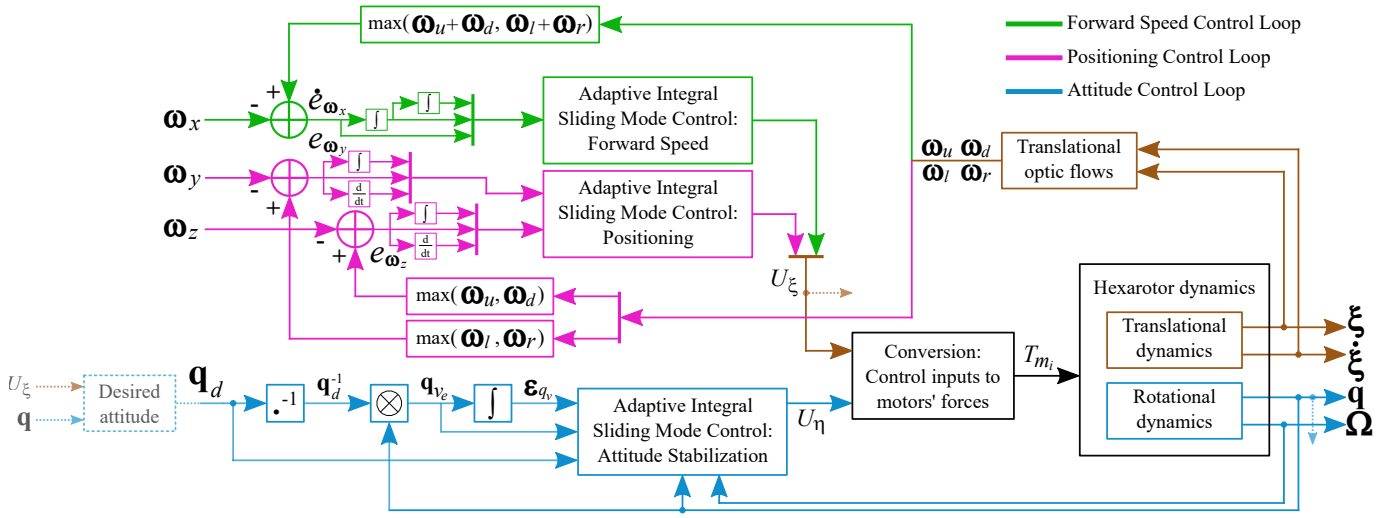

Figure 2. Control diagram including the triple OF regulation for FAH and UAH (faded elements are necessary for UAH).

A. Attitude stabilization

Consider the general case in which an hexarotor is meant to hold a given constant attitude described by the quaternion $\mathbf{q}_d = \begin{bmatrix} q_{0_d} & \mathbf{q}_{v_d}^T \end{bmatrix}^T$. The quaternion error and its derivative are:

$$\mathbf{q}_e = \mathbf{q}_d^{-1} \otimes \mathbf{q} = \begin{bmatrix} \mathbf{q}_d^T \\ \Xi_{\mathbf{q}_d}^T \end{bmatrix} \mathbf{q} = \begin{bmatrix} q_{0_e} & \mathbf{q}_{v_e}^T \end{bmatrix}^T \tag{14}$$

$$\dot{\mathbf{q}}_e = \frac{1}{2}\mathbf{q}_d^{-1} \otimes \dot{\mathbf{q}} = \frac{1}{2}\begin{bmatrix} \mathbf{q}_d^T \\ \Xi_{\mathbf{q}_d}^T \end{bmatrix} \Xi_{\mathbf{q}} \boldsymbol{\Omega} = \begin{bmatrix} \dot{q}_{0_e} & \dot{\mathbf{q}}_{v_e}^T \end{bmatrix}^T \tag{15}$$

where $\mathbf{q}_d^{-1} = \begin{bmatrix} q_{0_d} & -\mathbf{q}_{v_d}^T \end{bmatrix}^T$ stands as the conjugate of $\mathbf{q}_d$ and $\otimes$ denotes the quaternion multiplication. To achieve $\mathbf{q}_d$, AI-SMCs [24], [26] were implemented. In this vein, the sliding surfaces read as:

$$\boldsymbol{\sigma}_{\boldsymbol{\eta}} = \begin{bmatrix} \sigma_\phi & \sigma_\theta & \sigma_\psi \end{bmatrix}^T = \Upsilon_{\boldsymbol{\eta}} \dot{\mathbf{q}}_{v_e} + \Lambda_{\boldsymbol{\eta}} \mathbf{q}_{v_e} + \boldsymbol{\varepsilon}_{q_v} \tag{16}$$

with $\Upsilon_{\boldsymbol{\eta}} = \text{diag}\left(\upsilon_\phi, \upsilon_\theta, \upsilon_\psi\right), \Lambda_{\boldsymbol{\eta}} = \text{diag}\left(\lambda_\phi, \lambda_\theta, \lambda_\psi\right) \in \mathbb{R}^{3\times3}$ diagonal matrices containing the control gains $\upsilon, \lambda > 0$, and $\boldsymbol{\varepsilon}_{q_v} = \int \mathbf{q}_{v_e} dt$. The control input $\mathbf{U}_{\boldsymbol{\eta}} = \mathbf{u}_{\boldsymbol{\eta}_o} + \mathbf{u}_{\boldsymbol{\eta}_w} = \begin{bmatrix} U_\phi & U_\theta & U_\psi \end{bmatrix}^T \in \mathbb{R}^3$ shall mitigate the nominal dynamics by means of the term $\mathbf{u}_{\boldsymbol{\eta}_o}$, i.e. $\boldsymbol{\sigma}_{\boldsymbol{\eta}}^T \dot{\boldsymbol{\sigma}}_{\boldsymbol{\eta}} \leq 0$ or

$$\dot{\boldsymbol{\sigma}}_{\boldsymbol{\eta}} = \Upsilon_{\boldsymbol{\eta}} \ddot{\mathbf{q}}_{v_e} + \Lambda_{\boldsymbol{\eta}} \dot{\mathbf{q}}_{v_e} + \mathbf{q}_{v_e} = 0 \tag{17}$$

which yields to

$$\mathbf{u}_{\boldsymbol{\eta}_o} = -I\Xi_{\mathbf{q}}^T \left[\Xi_{\dot{\mathbf{q}}} \boldsymbol{\Omega} + 2\Xi_{\mathbf{q}_d} \Upsilon_{\boldsymbol{\eta}}^{-1} \left(\Lambda_{\boldsymbol{\eta}} \dot{\mathbf{q}}_{v_e} + \mathbf{q}_{v_e} \right) \right] + \boldsymbol{\Omega} \times (I\boldsymbol{\Omega})$$

The external disturbances $\boldsymbol{\rho}_{\boldsymbol{\Omega}}$ are mitigated by the influence of the term $\mathbf{u}_{\boldsymbol{\eta}_w}$ which is defined as

$$\mathbf{u}_{\boldsymbol{\eta}_w} = -I\Delta_{\boldsymbol{\eta}} \tanh\left(\boldsymbol{\sigma}_{\boldsymbol{\eta}} / \wp_{\boldsymbol{\eta}}\right) \tag{18}$$

with $\Delta_{\boldsymbol{\eta}} = \text{diag}\left(\delta_\phi, \delta_\theta, \delta_\psi\right)$ a matrix of adjustable control gains $\delta > 0$ and $\wp_{\boldsymbol{\eta}} > 0$ being a small real constant. The dynamics of $\Delta_{\boldsymbol{\eta}}$ depends on $\boldsymbol{\sigma}_{\boldsymbol{\eta}}$, such that:

$$\dot{\Delta}_{\boldsymbol{\eta}} = K_{\boldsymbol{\eta}}^{-1} \mathfrak{A}_{\boldsymbol{\sigma}_{\boldsymbol{\eta}}} \tag{19}$$

with $K_{\boldsymbol{\eta}} = \text{diag}\left(\kappa_\phi, \kappa_\theta, \kappa_\psi\right) \in \mathbb{R}^{3\times3}$ $(\kappa > 0)$ and $\mathfrak{A}_{\boldsymbol{\sigma}_{\boldsymbol{\eta}}} = \text{diag}\left(\left|\sigma_\phi\right|, \left|\sigma_\theta\right|, \left|\sigma_\psi\right|\right) \in \mathbb{R}^{3\times3}$. According to [26], a Lyapunov candidate function $V_{\boldsymbol{\eta}} \in \mathbb{R}$ may be:

$$V_{\boldsymbol{\eta}} = \frac{1}{2}\boldsymbol{\sigma}_{\boldsymbol{\eta}}^T \boldsymbol{\sigma}_{\boldsymbol{\eta}} + \frac{1}{2}\mathbf{I}_3^T \left(\Delta_{\boldsymbol{\eta}} - \Delta_{\boldsymbol{\eta}_d}\right)^T K_{\boldsymbol{\eta}} \left(\Delta_{\boldsymbol{\eta}} - \Delta_{\boldsymbol{\eta}_d}\right) \mathbf{I}_3 \tag{20}$$

where $\mathbf{I}_3 \in \mathbb{R}^3$ is a vector of ones and $|\Delta_{\boldsymbol{\eta}_d}| > |\boldsymbol{\rho}_{\boldsymbol{\Omega}}|$ the unknown terminal value reached by $\Delta_{\boldsymbol{\eta}}$, such that $\Delta_{\boldsymbol{\eta}} \to \Delta_{\boldsymbol{\eta}_d}$ as $t \to \infty$. Let the derivative of Eq. (20) be:

$$\dot{V}_{\boldsymbol{\eta}} = \boldsymbol{\sigma}_{\boldsymbol{\eta}}^T \dot{\boldsymbol{\sigma}}_{\boldsymbol{\eta}} + \mathbf{I}_3^T \left(\Delta_{\boldsymbol{\eta}} - \Delta_{\boldsymbol{\eta}_d}\right)^T \mathfrak{A}_{\boldsymbol{\sigma}_{\boldsymbol{\eta}}} \mathbf{I}_3 \tag{21}$$

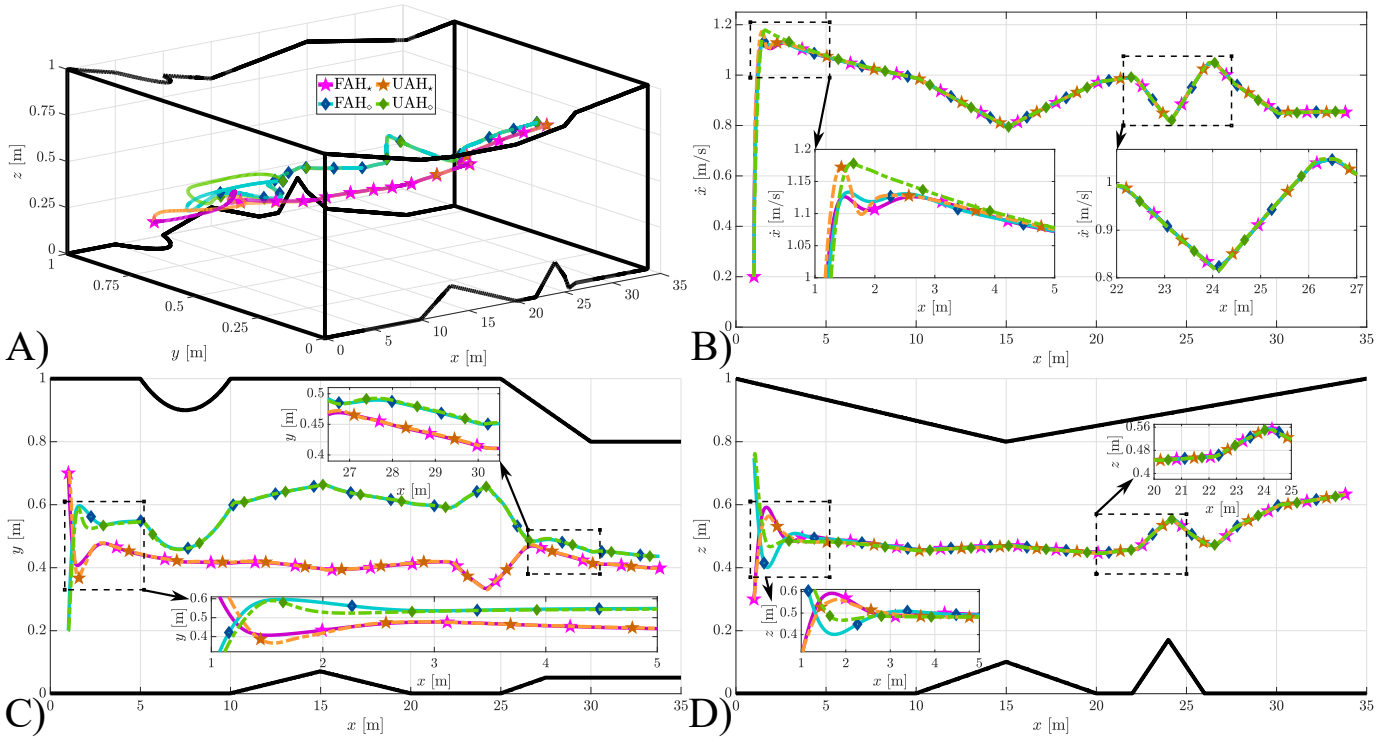

Figure 3. Comparison of the OF-based translational motion of the FAH and the UAH: A) 3D motion. B) Forward velocity. C) Position along y_I. D) Position along z_I

It is evident that $V_{\boldsymbol{\eta}} \geq 0$. Additionally, $\dot{V}_{\boldsymbol{\eta}} \leq 0$ since $\boldsymbol{\sigma}_{\boldsymbol{\eta}}^T \dot{\boldsymbol{\sigma}}_{\boldsymbol{\eta}} \leq 0$ by definition, $\Delta_{\boldsymbol{\eta}} \leq \Delta_{\boldsymbol{\eta}_d}$, $|\Delta_{\boldsymbol{\eta}_d}| > |\boldsymbol{\rho}_{\boldsymbol{\eta}}|$ and $\mathfrak{A}_{\boldsymbol{\sigma}_{\boldsymbol{\eta}}} \geq 0$. Thus, asymptotic local stability is guaranteed. For a detailed analysis, refer to [24], [26] and the corresponding references therein.

B. Triple optic flow regulation

The translational control was divided into: a forward speed control loop and a positioning control loop. The forward speed control loop regulates $\dot{x}$ in order to keep the maximum sum of the two diametrically opposed OFs constant and equal to the OF reference $\omega_x > 0$, such that the velocity error corresponds to $\dot{e}_{\omega_x} = \max(\omega_u + \omega_d, \omega_l + \omega_r) - \omega_x$. The positioning control loop regulates the distance w.r.t. the walls and the ground or the roof such that $\max(\omega_l, \omega_r) \to \omega_y$ and $\max(\omega_u, \omega_d) \to \omega_z$ where $\omega_{y,z} > 0$ are the desired OFs. In this sense, the errors are defined as:

$$\mathbf{e}_{\omega_{\boldsymbol{\xi}}} = \begin{bmatrix} e_{\omega_x} \\ e_{\omega_y} \\ e_{\omega_z} \end{bmatrix} = \begin{bmatrix} \int (\max(\omega_u + \omega_d, \omega_l + \omega_r) - \omega_x) dt \\ \max(\omega_l, \omega_r) - \omega_y \\ \max(\omega_u, \omega_d) - \omega_z \end{bmatrix} \tag{22}$$

According to [25], $\omega_x = 4.57$ rad/s and $\omega_{y,z} = 2.4$ rad/s correspond to what has been registered during experiments on freely flying bees. Thus, these values were used as reference in the simulations. For instance, the sliding surfaces are:

$$\boldsymbol{\sigma}_{\boldsymbol{\xi}} = \begin{bmatrix} \sigma_x & \sigma_y & \sigma_z \end{bmatrix}^T = \Upsilon_{\boldsymbol{\xi}} \dot{\mathbf{e}}_{\omega_{\boldsymbol{\xi}}} + \Lambda_{\boldsymbol{\xi}} \mathbf{e}_{\omega_{\boldsymbol{\xi}}} + \boldsymbol{\varepsilon}_{\omega_{\boldsymbol{\xi}}} \tag{23}$$

with $\Upsilon_{\boldsymbol{\xi}} = \text{diag}(\upsilon_x, \upsilon_y, \upsilon_z), \Lambda_{\boldsymbol{\xi}} = \text{diag}(\lambda_x, \lambda_y, \lambda_z) \in \mathbb{R}^{3\times 3}$ diagonal matrices containing the control gains $\upsilon, \lambda > 0$, and $\boldsymbol{\varepsilon}_{\omega_{\boldsymbol{\xi}}} = \int \mathbf{e}_{\omega_{\boldsymbol{\xi}}} dt$.

Since $\omega_j > 0$, an additional step must be considered to define the actual control input $\mathbf{U}_{\boldsymbol{\xi}} = [U_x \; U_y \; U_z]^T \in \mathbb{R}^3$. In this sense, let the auxiliary control input $\mathbf{u}_{\boldsymbol{\xi}} = [u_x \; u_y \; u_z]^T \in \mathbb{R}^3$ be:

$$\mathbf{u}_{\boldsymbol{\xi}} = -\Upsilon_{\boldsymbol{\xi}}^{-1} \left(\Lambda_{\boldsymbol{\xi}} \dot{\mathbf{e}}_{\omega_{\boldsymbol{\xi}}} + \mathbf{e}_{\omega_{\boldsymbol{\xi}}} \right) - \Delta_{\boldsymbol{\xi}} \tanh\left(\boldsymbol{\sigma}_{\boldsymbol{\xi}} / \wp_{\boldsymbol{\xi}} \right) \tag{24}$$

such that $\wp_{\boldsymbol{\xi}} > 0$ is a small real constant and $\Delta_{\boldsymbol{\xi}} = \text{diag}(\delta_x, \delta_y, \delta_z) \in \mathbb{R}^{3\times 3}$ is an adjustable control gain matrix whose dynamics is defined as:

$$\dot{\Delta}_{\boldsymbol{\xi}} = K_{\boldsymbol{\xi}}^{-1} \mathfrak{A}_{\boldsymbol{\sigma}_{\boldsymbol{\xi}}} \tag{25}$$

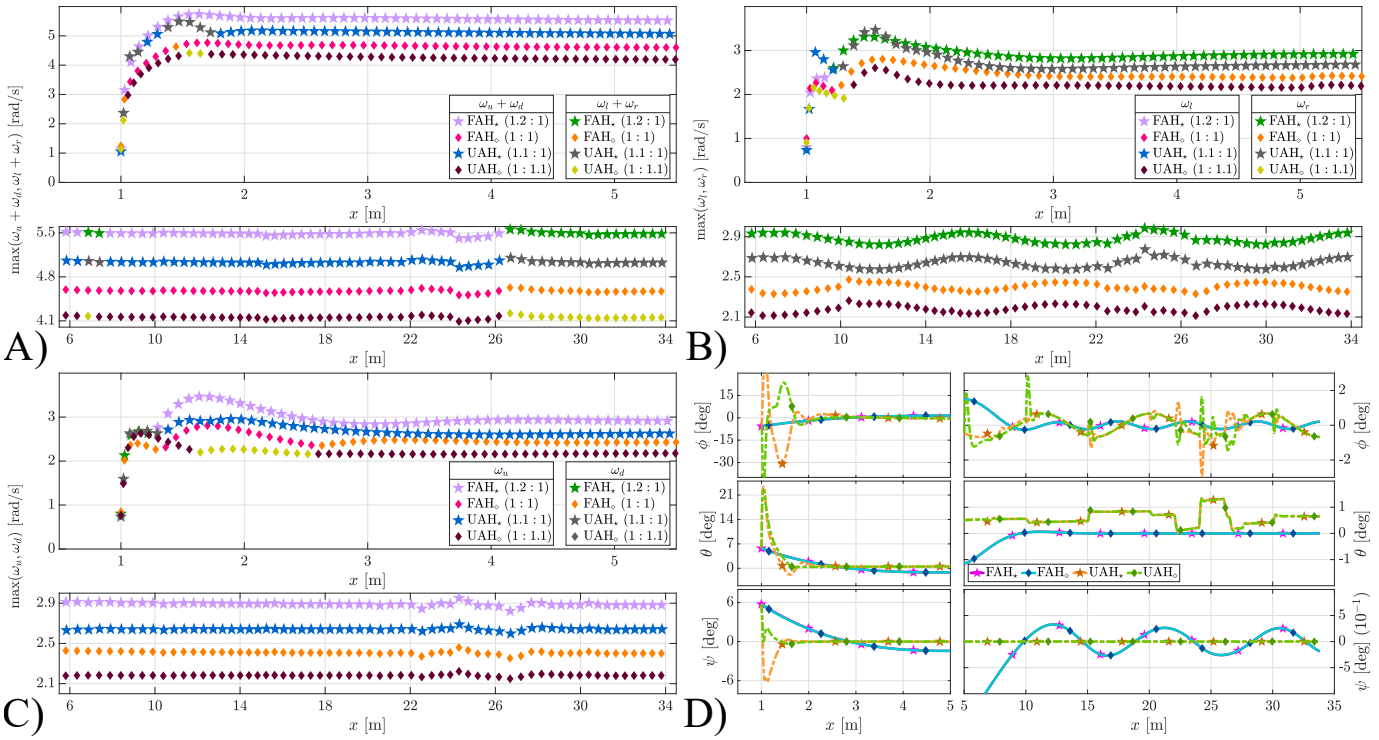

Figure 4. Comparison of the OF regulations and the attitude of the FAH and the UAH: A) Maximum sum of the two diametrically opposed OFs. B) Maximum lateral OFs. C) Maximum vertical OFs. D) Attitude. (some OFs have been scaled).

with $K_{\boldsymbol{\xi}} = \text{diag}\,(\kappa_x, \kappa_y, \kappa_z) \in \mathbb{R}^{3\times3}$ (such that $\kappa > 0$) and $\mathfrak{A}_{\boldsymbol{\sigma_\xi}} = \text{diag}\left(|\sigma_x|, |\sigma_y|, |\sigma_z|\right) \in \mathbb{R}^{3\times3}$. The stability analysis can be performed as in the previous case.
Finally, according to the largest of the OFs, $\mathbf{U}_{\boldsymbol{\xi}}$ is written as:

$$\mathbf{U}_{\boldsymbol{\xi}} = \begin{bmatrix} U_x \\ U_y \\ U_z \end{bmatrix} \quad \text{with} \quad \begin{aligned} U_x &= mu_x \\ U_y &= \begin{cases} mu_y & \omega_l > \omega_r \\ -mu_y & \text{else} \end{cases} \\ U_z &= \begin{cases} m\,(u_z + g) & \omega_u > \omega_d \\ -m\,(u_z - g) & \text{else} \end{cases} \end{aligned} \tag{26}$$

To compute the force T_{m_i} that each motor must exert, α_i and β_i shall be firstly set. Afterwards, it is sufficient to relate Eqs. (3) and (6) to Eq. (26) and $\mathbf{U}_{\boldsymbol{\eta}}$, respectively, such that $\boldsymbol{\tau}_{\boldsymbol{\xi}} = \mathbf{U}_{\boldsymbol{\xi}}$ and $\boldsymbol{\tau}_{\boldsymbol{\Omega}} = \mathbf{U}_{\boldsymbol{\eta}}$, to provide a system of equations that can be solved for T_{m_i} [16], [17], [18].

IV. Results

To validate the navigation strategy, the hexarotors (FAH and UAH) introduced in Section II were considered in simulations. The geometrical parameters and properties of the hexarotors, alongside the control gains, are presented in Table I.
Both hexarotors were meant to navigate a straight corridor with irregular surfaces and small time-varying external disturbances. It was supposed that the vehicles entered the corridor with an initial velocity $\dot{x}_0 = 0.2$ [m/s] and that the navigation strategy started to take place at $x_0 = 1$ [m]. The initial attitude was set at $\boldsymbol{\eta}_0 \approx 5.7296\,[-1\ 1\ 1]^T$ [deg] or $\mathbf{q}_0 \approx [0.9961\ \ -0.0523\ 0.0474\ 0.0523]^T$. Regarding the initial position on the plane $y_I - z_I$, two different points were randomly chosen: ($\star$) $(y_{0_\star}, z_{0_\star}) = (0.7, 0.3)$ [m] and ($\diamond$) $(y_{0_\diamond}, z_{0_\diamond}) = (0.2, 0.75)$ [m] ($\star$ and $\diamond$ are used as sub-indices and markers to refer to these positions).
From Fig. 3, which shows the translational behavior of the hexarotors, one can observe that the narrower the corridor, the slower the vehicle travels, as in [25]. Yet, at the initial stage, the positioning of the vehicles differed from the expectations since the hexarotors were supposed to approach to the closest surfaces and follow them. The latter may occur due to the initial overshoot which causes them to go beyond the proper position such that the initial furthest surface becomes the closest at this point, phenomena that may occurs several times during the transient. Nevertheless, during the steady-state phase, the hexarotors followed correctly the corresponding surfaces, which was reinforced by the successfully regulation of the OFs as depicted in Fig. 4.
The slight difference between the transient response of the FAH and that of the UAH can be attributed to the UAH under-actuation.

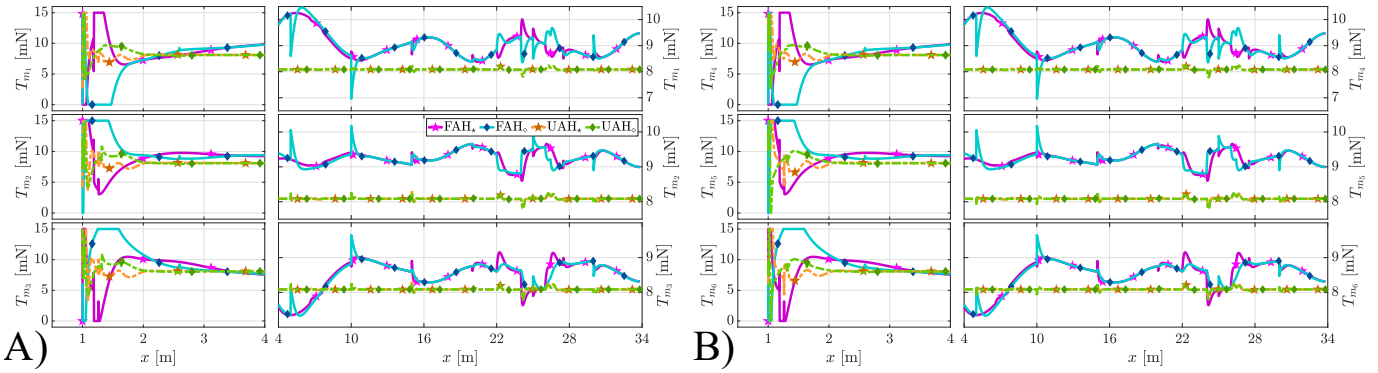

Figure 5. Comparison of the forces of the FAH and the UAH: A) Rotors 1, 2 and 3. B) Rotors 4, 5 and 6.

The UAH translational dynamics may be slower in comparison with that of the FAH since, in the case of the UAH, the rotational dynamics must be faster than that of translation. The altitude and forward velocity controls may be equally impacting due to couplings related to the overall dynamics and the OFs. A proper selection of the control gains could solve these issues. According to Fig. 4, it is possible for the FAH to converge to the desired attitude $\mathbf{q}_s$ which ensures the correct orientation of the OF sensors. The attitude of the UAH may experience an aggressive response in the transient phase which suggests that the usage of sensors stabilizers is necessary in order to ensure a correct OF sensing to overcome this initial stage. In steady state, the UAH and the FAH can be considered to act in a quasi-hover state.

The navigation task is a direct result of a proper forces exertion (see Fig. 5). In this sense, it may be obvious that the FAH tends to consume more energy in comparison with the UAH due to the tilted rotors configuration yet, one shall consider the additional mass of the gimbal system which may be treated as a greater disturbance implying that more energy is consumed. Nonetheless, Figs. 3 and 4 suggest that this power consumption issue is compensated by an accuracy gain. One should be able to find the perfect balance between power consumption and accuracy/reliability according to the requirements of the operation. However, the simulation results suggest that the strategy can be performed by both hexarotors.

V. Conclusion

In this paper, a corridor honeybee-inspired navigation strategy based on OF has been adapted to one of the most common UAVs structure. The results provided by numerical simulations have shown that the implementation of AI-SMCs permits the vehicles to navigate through a straight corridor while reacting actively to the irregularities of the surfaces, similar to what has been observed on bees.

Future works will include the rotational optic flow perturbation while rotating and an accurate tuning of the controllers' gains

Table I
Simulation parameters

Hexarotor platform		
Property/ Parameter	**FAH**	**UAH**
m [kg]	0.05	
$I_x,\ I_y,\ I_z$ [kg mm^2]	140, 197, 250	
ℓ [m]	0.04	
ζ [m]	0.3	
α_i [deg]	$(-1)^i$ 25	0
β_i [deg]	0	
T_m^u (T_{m_i} upper bound) [N]	0.015	
g [m/s^2]	9.81	
Control gains		
Gains	**FAH**	**UAH**
$\upsilon_x,\ \lambda_x,\ \delta_{x_0},\ \kappa_x$	1.1, 2, 0.15, 1000	
$\upsilon_y,\ \lambda_y,\ \delta_{y_0},\ \kappa_y$	0.5, 0.45, 0.05, 1000	
$\upsilon_z,\ \lambda_z,\ \delta_{z_0},\ \kappa_z$	0.5, 0.25, 2, 1000	
$\upsilon_\phi,\ \lambda_\phi,\ \delta_{\phi_0},\ \kappa_\phi$	0.01, 2, 1, 1	0.002, 0.075, 0.01, 1000
$\upsilon_\theta,\ \lambda_\theta,\ \delta_{\theta_0},\ \kappa_\theta$		
$\upsilon_\psi,\ \lambda_\psi,\ \delta_{\psi_0},\ \kappa_\psi$		0.0005, 0.175, 0.01, 1000
$\wp_{\boldsymbol{\xi}},\ \wp_{\boldsymbol{\eta}}$	0.1, 0.01	

for the vehicle. Different control approaches will be equally considered and other bio-inspired techniques, related but not limited to data fusion and odometry, may be implemented in order to improve the reliability of the vehicle in operation. Upcoming work comprehends real experimentation in complex scenarios to validate the concept.

REFERENCES

[1] O. Alparslan and O. Cetin, "Fast and effective identification of window and door openings for uavs' indoor navigation," in *2021 International Conference on Unmanned Aircraft Systems (ICUAS)*. IEEE, 2021, pp. 175–181.

[2] A. Garcia, S. S. Mittal, E. Kiewra, and K. Ghose, "A convolutional neural network vision system approach to indoor autonomous quadrotor navigation," in *2019 International Conference on Unmanned Aircraft Systems (ICUAS)*. IEEE, 2019, pp. 1344–1352.

[3] N. Urieva, J. McDonald, T. Uryeva, A. S. R. Ramos, and S. Bhandari, "Collision detection and avoidance using optical flow for multicopter uavs," in *2020 International Conference on Unmanned Aircraft Systems (ICUAS)*. IEEE, 2020, pp. 607–614.

[4] A. Miller, B. Miller, A. Popov, and K. Stepanyan, "Optical flow as a navigation means for uav," in *2018 Australian & New Zealand Control Conference (ANZCC)*. IEEE, 2018, pp. 302–307.

[5] M. V. Srinivasan, S. Zhang, M. Altwein, and J. Tautz, "Honeybee navigation: Nature and calibration of the" odometer"," *Science*, vol. 287, no. 5454, pp. 851–853, 2000.

[6] R. Savita and M. Trigunayat, "First checklist of observations on the moth diversity (lepidoptera: Heterocera) in and around jaipur city, rajasthan, india," *International Journal of Entomology Research*, vol. 6, no. 2, pp. 39–45, 2021.

[7] F. L. Roubieu, J. R. Serres, F. Colonnier, N. Franceschini, S. Viollet, and F. Ruffier, "A biomimetic vision-based hovercraft accounts for bees' complex behaviour in various corridors," *Bioinspiration & biomimetics*, vol. 9, no. 3, p. 036003, 2014.

[8] N. Franceschini, F. Ruffier, and J. Serres, "A bio-inspired flying robot sheds light on insect piloting abilities," *Current Biology*, vol. 17, no. 4, pp. 329–335, 2007.

[9] F. Expert and F. Ruffier, "Flying over uneven moving terrain based on optic-flow cues without any need for reference frames or accelerometers," *Bioinspiration & biomimetics*, vol. 10, no. 2, p. 026003, 2015.

[10] L. Bergantin, T. Raharijaona, and F. Ruffier, "Estimation of the distance from a surface based on local optic flow divergence," in *2021 International Conference on Unmanned Aircraft Systems (ICUAS)*. IEEE, 2021, pp. 1291–1298.

[11] L. Bergantin, N. Harbaoui, T. Raharijaona, and F. Ruffier, "Oscillations make a self-scaled model for honeybees' visual odometer reliable regardless of flight trajectory," *Journal of the Royal Society Interface*, vol. 18, no. 182, p. 20210567, 2021.

[12] M. Nadour, M. Boumehraz, L. Cherroun, and V. Puig, "Mobile robot visual navigation based on fuzzy logic and optical flow approaches," *International Journal of System Assurance Engineering and Management*, vol. 10, no. 6, pp. 1654–1667, 2019.

[13] G. Allasia, A. Rizzo, and K. Valavanis, "Quadrotor uav 3d path planning with optical-flow-based obstacle avoidance," in *2021 International Conference on Unmanned Aircraft Systems (ICUAS)*. IEEE, 2021, pp. 1029–1036.

[14] L. Meng, S. Ren, G. Tang, C. Yang, and W. Yang, "Uav sensor spoofing detection algorithm based on gps and optical flow fusion," in *Proceedings of the 2020 4th International Conference on Cryptography, Security and Privacy*, 2020, pp. 146–151.

[15] F. Fanin and J.-H. Hong, "Visual inertial navigation for a small uav using sparse and dense optical flow," in *2019 Workshop on Research, Education and Development of Unmanned Aerial Systems (RED UAS)*. IEEE, 2019, pp. 206–212.

[16] S. Rajappa, M. Ryll, H. H. Bülthoff, and A. Franchi, "Modeling, control and design optimization for a fully-actuated hexarotor aerial vehicle with tilted propellers," in *2015 IEEE international conference on robotics and automation (ICRA)*. IEEE, 2015, pp. 4006–4013.

[17] D. Bicego, J. Mazzetto, R. Carli, M. Farina, and A. Franchi, "Nonlinear model predictive control with enhanced actuator model for multi-rotor aerial vehicles with generic designs," *Journal of Intelligent & Robotic Systems*, vol. 100, no. 3, pp. 1213–1247, 2020.

[18] J. A. Bezerra and D. A. Santos, "On the guidance of fully-actuated multirotor aerial vehicles under control allocation constraints using the receding-horizon strategy," *ISA transactions*, 2021.

[19] J. J. Castillo-Zamora, K. A. Camarillo-Gómez, G. I. Pérez-Soto, and J. Rodríguez-Reséndiz, "Comparison of pd, pid and sliding-mode position controllers for v–tail quadcopter stability," *IEEE Access*, vol. 6, pp. 38 086–38 096, 2018.

[20] M. F. Santos, L. M. Honório, E. B. Costa, E. J. Oliveira, and J. P. P. G. Visconti, "Active fault-tolerant control applied to a hexacopter under propulsion system failures," in *2015 19th international conference on system theory, control and computing (ICSTCC)*. IEEE, 2015, pp. 447–453.

[21] P. Poksawat and L. Wang, "Automatic tuning of hexacopter attitude control systems with experimental validation," in *2017 21st International Conference on System Theory, Control and Computing (ICSTCC)*. IEEE, 2017, pp. 753–758.

[22] R. Campa, K. Camarillo, and M. Ceccarelli, "Unit quaternions: A mathematical tool for modeling, path planning and control of robot manipulators," *Robot manipulators, M. Ceccarelli (ed.), In-Teh*, pp. 21–48, 2008.

[23] J. Alvarez-Muñoz, J. Castillo-Zamora, J. Escareno, I. Boussaada, F. Méndez-Barrios, and O. Labbani-Igbida, "Time-delay control of a multi-rotor vtol multi-agent system towards transport operations," in *2019 International Conference on Unmanned Aircraft Systems (ICUAS)*. IEEE, 2019, pp. 276–283.

[24] J. Alvarez-Muñoz, J. Chevalier, J. J. Castillo-Zamora, and J. Escareno, "Distributed event-based sliding-mode consensus control in dynamic formation for vtol-uavs," in *2021 International Conference on Unmanned Aircraft Systems (ICUAS)*. IEEE, 2021, pp. 1364–1373.

[25] G. Portelli, J. Serres, F. Ruffier, and N. Franceschini, "Modelling honeybee visual guidance in a 3-d environment," *Journal of Physiology-Paris*, vol. 104, no. 1-2, pp. 27–39, 2010.

[26] J. Castillo-Zamora, J. Escareno, I. Boussaada, O. Labbani, and K. Camarillo, "Modeling and control of an aerial multi-cargo system: Robust acquiring and transport operations," in *2019 18th European Control Conference (ECC)*. IEEE, 2019, pp. 1708–1713.